Photoimprint Photoacoustic Microscopy for Three-Dimensional Label-Free Subdiffraction Imaging

Junjie Yao, Lidai Wang, Chiye Li, Chi Zhang, and Lihong V. Wang[*]

*Optical Imaging Laboratory, Department of Biomedical Engineering, Washington University in St. Louis,
St. Louis, Missouri 63130, USA*

Subdiffraction optical microscopy allows the imaging of cellular and subcellular structures with a resolution finer than the diffraction limit. Here, combining the absorption-based photoacoustic effect and intensity-dependent photobleaching effect, we demonstrate a simple method for subdiffraction photoacoustic imaging of both fluorescent and nonfluorescent samples. Our method is based on a double-excitation process, where the first excitation pulse partially and inhomogeneously bleaches the molecules in the diffraction-limited excitation volume, thus biasing the signal contributions from a second excitation pulse striking the same region. The differential signal between the two excitations preserves the signal contribution mostly from the center of the excitation volume, and dramatically sharpens the lateral resolution. Moreover, due to the nonlinear nature of the signal, our method offers an inherent optical sectioning capability, which is lacking in conventional photoacoustic microscopy. By scanning the excitation beam, we performed three-dimensional subdiffraction imaging of varied fluorescent and nonfluorescent species. As any molecules have absorption, this technique has the potential to enable label-free subdiffraction imaging, and can be transferred to other optical imaging modalities or combined with other subdiffraction methods.

In recent years, by breaking the diffraction limit, subdiffraction optical microcopy has revolutionized fundamental biological studies. Generally speaking, subdiffraction techniques fall into two broad categories: so-called "pattern excitation" approaches and single-molecule localization approaches [1]. In the method we describe here, the resolution enhancement is based on the excitation nonlinearity of the photobleaching effect, a common phenomenon in optical imaging which is otherwise regarded as harmful [2,3]. The photobleaching effect depends strongly on the excitation intensity for both fluorescent and nonfluorescent species, which enables subdiffraction imaging by spatially trimming the excitation volume to a subdiffraction size [4–6]. Since all molecules are optically absorbing at selected wavelengths, photoacoustic (PA) imaging, which acoustically probes optical absorption contrast in biological tissue, can potentially image all molecules, endogenous and exogenous [7]. Therefore, the combination of the photobleaching effect and photoacoustic imaging can potentially achieve subdiffraction imaging over a wide range of species.

Photoacoustic imaging is based on the photoacoustic effect. The principle of photobleaching-based photoimprint subdiffraction PA microscopy (PI-PAM) is illustrated in Fig. 1(a). When a Gaussian-shape diffraction-limited excitation spot strikes on densely distributed absorbers, the generated PA signal is a summation of the contributions from all absorbers inside the excitation spot [Fig. 1(a), left panel]. After the first excitation, the absorbers inside the excitation spot are inhomogeneously bleached, depending on the local excitation intensity [Fig. 1(a), middle panel]. Therefore, the reduction of absorption in the center of the excitation spot is greater than that in the periphery. As a result, when the second pulse excites the same region, the center portion contributes less to the second PA signal than the periphery. The difference between the two PA signals not only reflects the excitation intensity profile, but also incorporates the absorption reduction distribution [Fig. 1(a), right panel], which therefore sharpens the center of the focus. This concept of enhancement in the lateral resolution is elucidated in Fig. 1(b). In summary, while each PA signal is linear to the excitation intensity, the differential signal is nonlinear to the excitation intensity. This is the physical basis of our method.

The contrast of the PI-PAM comes from the differential signal between two adjacent frames, expressed as (see Supplemental Material [8], Note 1, for more derivation)

$$\Delta P = P_{i-1} - P_i \propto k\Gamma\eta_{\text{th}}N_0 I^{b+1}, \tag{1}$$

where P_i is the signal amplitude detected by the ultrasonic transducer with the ith excitation, Γ is the Grueneisen coefficient, η_{th} is the percentage of the absorbed photon energy that is converted into heat, N_0 is the initial number of molecules, I is the excitation intensity, and b is the power dependence of the photobleaching rate on the excitation intensity. Equation (1) indicates that, on the one hand, the PI-PAM signal is linear to the optical absorption, which maintains its functional imaging capability, such as oxygen
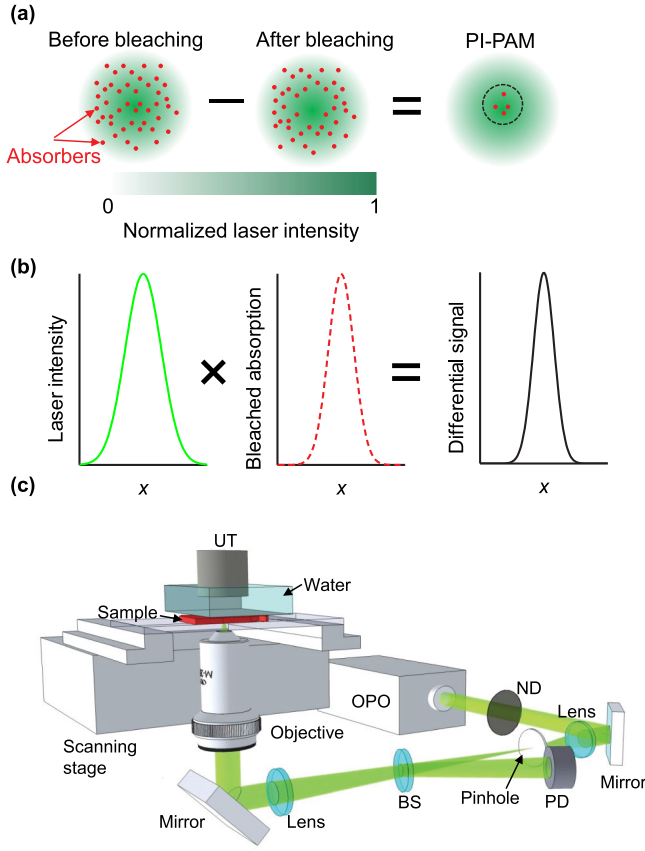
FIG. 1 (color online). Photoimprint photoacoustic microscopy (PI-PAM). (a) Principle of PI-PAM. The differential signal between before- (left panel) and after-bleaching (middle panel) images results in a smaller effective excitation size, as shown by the dashed circle in the right panel. (b) Illustration of the lateral resolution enhancement by PI-PAM. The effective PSF is the product of the excitation PSF and the photobleaching profile. (c) Schematic of the central components of a PI-PAM system. Beam sampler (BS), neutral density filter (ND), photodiode (PD), optical parametric oscillator (OPO), and ultrasonic transducer (UT).

saturation measurement. On the other hand, the PI-PAM signal is nonlinear to the excitation intensity, which enables the subdiffraction imaging capability.

If the excitation profile can be approximated by a Gaussian function, we obtain the full-width at half-maximum (FWHM) of the lateral point spread function (PSF) of the imaging system as (see Supplemental Material [8], Note 2, for more detailed derivation)

$$\text{FWHM}_r = \sqrt{\frac{2\ln 2}{1+b}} w_e \approx \frac{0.51}{\sqrt{1+b}} \frac{\lambda_0}{\text{NA}}, \qquad (2)$$

where r is the radial distance from the center of the Airy disk, w_e is the Gaussian width of the excitation beam where the beam intensity drops to $1/e^2$ of its center value, λ_0 is the

excitation wavelength and NA is the numerical aperture of the objective. Equation (2) indicates that the effective PSF [Fig. 1(b), right panel] of the system is sharper than the initial diffraction-limited excitation PSF [Fig. 1(b), left panel] by a factor of $\sqrt{1+b}$.

Similarly, the axial resolution of PI-PAM for point targets is given by the FWHM of the axial PSF as (see Supplemental Material [8], Note 3, for more detailed derivation)

$$\begin{aligned}\text{FWHM}_z^{\text{point}} &= 2\sqrt{2^{1/(1+b)} - 1}\, z_R \\ &= 1.8\sqrt{2^{1/(1+b)} - 1}\, \frac{\lambda_0}{\text{NA}^2}, \qquad (3)\end{aligned}$$

where z is the axial distance from the focal plane and Z_R is the Rayleigh range of the Gaussian beam. Equation (3) shows that, by sharpening the optical focal zone, PI-PAM provides an axial resolution improvement by a factor of $1/\sqrt{2^{1/(1+b)} - 1}$ over conventional PAM for point targets.

For planar (or wide) targets, conventional PA microscopy (PAM) lacks sectioning capability because its axial PSF is constant. By contrast, for PI-PAM, the optical sectioning capability can be expressed as the FWHM of the axial PSF:

$$\text{FWHM}_z^{\text{planar}} = 2\sqrt{2^{1/b} - 1}\, z_R = 1.8\sqrt{2^{1/b} - 1}\, \frac{\lambda_0}{\text{NA}^2}. \quad (4)$$

Equation (4) shows that the optical sectioning capability of PI-PAM also depends on the intensity power dependence of the photobleaching rate.

The photoimprint PA microscopy system is illustrated in Fig. 1(c) (for more details, see Supplemental Material [8], methods and Fig. 1). Briefly stated, an OPO (optical parametric oscillator) laser with a wavelength tuning range of 210–2600 nm serves as the excitation source. After spatial filtering, the beam is focused into the sample by a 1.4 NA (numerical aperture) oil-immersion objective. The photoacoustic waves are detected by a focused ultrasonic transducer (customized with 40 MHz central frequency, 80% bandwidth, and 0.50 NA), which is placed confocally with the objective and coupled by water. A customized LABVIEW program synchronizes the entire system. PI-PAM imaging can be performed point by point (*A*-scan mode), cross section by cross section (*B*-scan mode), or volume by volume (*C*-scan mode). If not otherwise mentioned, *A*-scan mode was used for the experiments in this Letter. The second pulse is a separate event, which follows the first pulse that partially bleaches the absorbers. To ensure that the PA signals from two consecutive pulses do not temporally overlap, the time interval between the two pulses should be at least a few microseconds. In practice, we make sure that the two pulses are more than 1 ms

apart. To achieve sufficient detection sensitivity, typically more than 200 frames were acquired for each experiment.

To improve the signal-to-noise ratio (SNR) in practice, we took the difference between frames that are half of the total number of frames apart, and then averaged all the differential images (see Supplemental Material [8], Note 4, for more detailed derivation). Assume that the total number of frames is M, the true signal difference between adjacent frames is ΔS, and the standard deviation of the white noise is σ. Approximately, averaging of the differential signals between frames that are $M/2$ apart yields a SNR of

$$\mathrm{SNR}_{M/2} = \frac{M}{4} \sqrt{M} \frac{\Delta S}{\sigma}. \qquad (5)$$

The SNR ratio between PI-PAM and conventional PAM is given by

$$R_{\mathrm{SNR}} = \frac{\mathrm{SNR}_{\mathrm{PI\text{-}PAM}}}{\mathrm{SNR}_{\mathrm{C\text{-}PAM}}} = \frac{q}{2(2-q)}. \qquad (6)$$

Equation (6) suggests that the SNR advantage of conventional PAM decreases as the bleached percentage q increases. The SNR of PI-PAM can be improved by increasing the bleaching percentage with either more imaging frames or stronger excitation intensity.

Using this setup, we first studied the photobleaching characteristics of several biological and nonbiological samples commonly used in PA imaging, including red blood cells, B16 melanoma cells, black ink, gold nanoparticles, and graphite (Supplemental Material [8], Fig. 2). An exponential-decay model was used to fit for the photobleaching rate at different excitation intensities. The power dependence of each material on the excitation intensity determines the expected resolution improvement. Among the test materials, gold nanoparticles have the highest power dependence of 4.0, which is expected to improve the lateral resolution to ~87 nm.

The lateral resolution enhancement of PI-PAM over conventional PA microscopy is presented in Fig. 2. A sharp blade edge coated with hemoglobin was imaged at 532 nm, and the corresponding line spread function was fitted to compute the lateral resolution [Fig. 2(a)]. With an objective NA of 1.4, conventional PAM achieved a lateral resolution of 200 nm, in agreement with the diffraction limit. By contrast, PI-PAM achieved a subdiffraction lateral resolution of 120 nm, a 1.7-fold improvement. Since the photobleaching of hemoglobin has a power dependence of 2.2 on the excitation intensity, the measured resolution is close to the expected value of 112 nm. To demonstrate the imaging performance, conventional PAM and PI-PAM were applied to image a monolayer of 200-nm-diameter densely packed red-dyed microspheres [Fig. 2(b)]. The red dye's photobleaching property was similar to that of hemoglobin. The images show that the microspheres
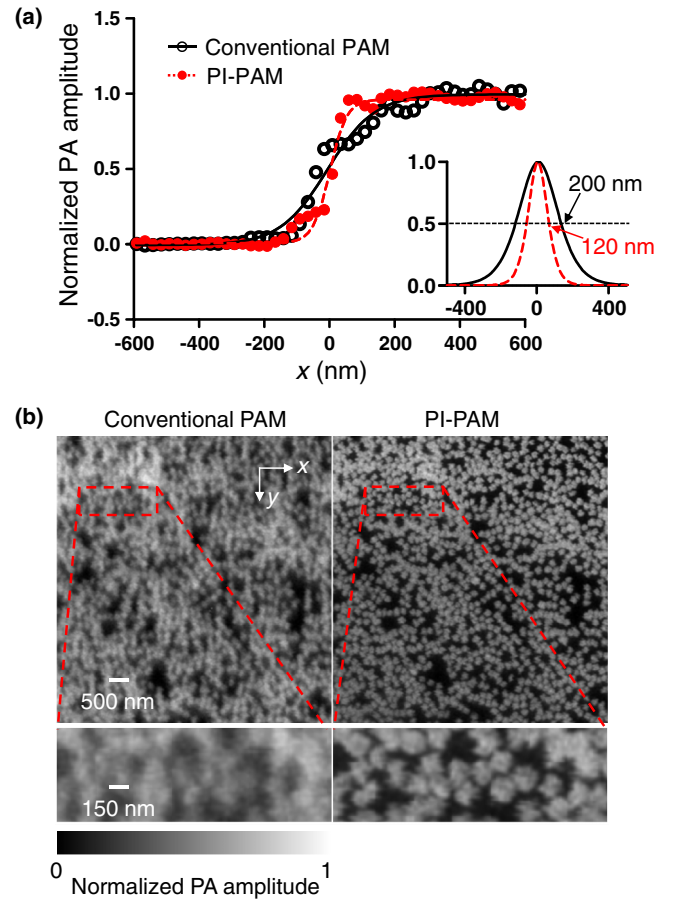

FIG. 2 (color online). Lateral resolution enhancement by PI-PAM. (a) Edge spread function of conventional PAM and PI-PAM, using a sharp blade edge coated with hemoglobin. (b) A cluster of red-dyed microspheres with nominal diameters of 200 nm, as imaged by conventional PAM (left) and PI-PAM (right). The dashed boxes in the top row were magnified and shown in the bottom row.

were much better resolved by PI-PAM, which confirmed the lateral resolution improvement.

We further demonstrate the subdiffraction imaging capability of PI-PAM on both nonbiological and biological samples (Fig. 3). We compared conventional PAM and PI-PAM images of 150-nm diameter gold nanoparticles [Fig. 3(a) and movie S1 in the Supplemental Material [8]]. Two closely located nanoparticles, 270 nm apart, were clearly resolved by PI-PAM but barely resolved by conventional PAM [Fig. 3(a), insets]. The line profile across one nanoparticle shows a full width at half maximum of 170 nm [Fig. 3(a), right]. Because the line profile is a convolution of the effective PSF of the system with the particle absorption profile, deconvolution of the line profile using the Gaussian approximation results in an effective lateral resolution of 80 nm for PI-PAM, consistent with the expected value. We also imaged a fixed B16 melanoma cell [Fig. 3(b) and movie S2 [8]]. The PI-PAM image is clearly superior in resolution. Small dendrites in the melanoma cell
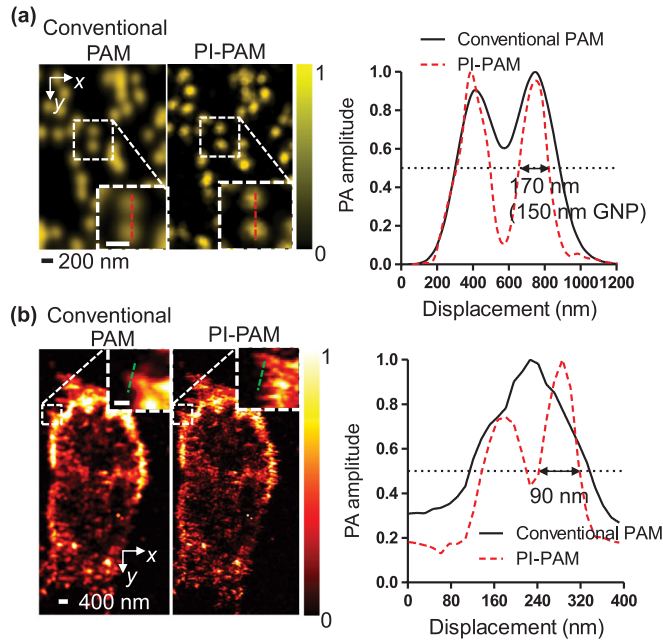
FIG. 3 (color online).   PI-PAM imaging of gold nanoparticles and melanoma cells with enhanced lateral resolution. (a)–(b) 150-nm diameter gold nanoparticles (a), and a B16 melanoma cell (b) imaged by conventional PAM (left column) and PI-PAM (middle column). The normalized signal amplitude profiles along the dashed lines are shown in the right column. Insets show magnified views of the marked areas. The scale bars for the insets are 200 nm.

that are less than 100 nm apart can be clearly separated by PI-PAM [Fig. 3(b), insets].

The other important advantage offered by PI-PAM is its optical sectioning capability, providing axial resolution for not only point targets but also targets that are large relative to the lateral resolution. As shown by Eq. (4), the axial resolution for planar targets originates from the nonuniform light intensity along the axial beam axis. The light intensity is stronger at the focal plane. Therefore, the absorbers at the focal plane are bleached more than the absorber farther away from the focal plane. The difference of the PA signals before and after bleaching is thus axial-position dependent. This dependence results in the axial resolution for planar targets. A simple illustration is shown in Fig. 4(a). Like the lateral resolution enhancement, the sectioning strength of PI-PAM is determined by the power dependence of the photobleaching rate on the excitation intensity. For example, with a linear dependence, PI-PAM should achieve a sectioning capability comparable with that of confocal microscopy. We first quantified the sectioning by using a layer of dried hemoglobin (∼150 nm in thickness) [Fig. 4(b) and Supplemental Material, Fig. 4 [8]]. While the signal strength in conventional PAM decayed very slowly, the signal strength in PI-PAM sharply dropped as the sample moved out of focus. The FWHM of the signal profile in PI-PAM suggests a sectioning capability of
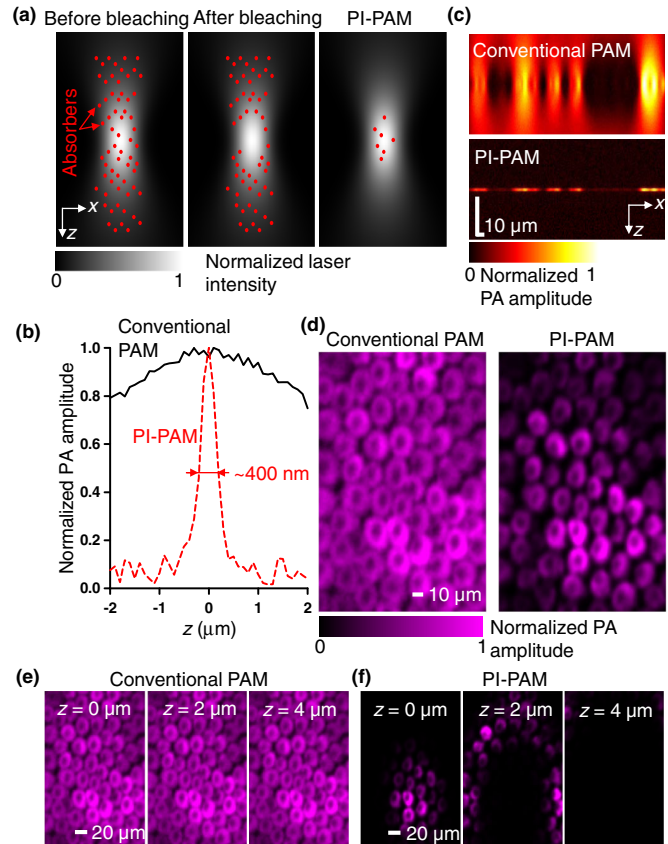

FIG. 4 (color online).   Optical sectioning capability of PI-PAM. (a) Illustration of the optical sectioning capability provided by PI-PAM. The differential signal of the before- (left) and after-bleaching (middle) images largely removes the out-of-focus contributions. (b) The axial point spread function measured on a thin-layer hemoglobin sample. (c) Orthogonal projections of single layer red blood cells imaged by conventional PAM and PI-PAM at varying axial positions. (d)–(f) Subdiffraction imaging of live rose petal epidermal cells at 570 nm. The sample was z scanned with a step size of 0.5 μm. Maximum-amplitude projections (d) were extracted from the z-stacked images (e)–(f).

370 nm after deconvolution with the absorption profile of the sample, close to the expected value (320 nm). Accordingly, a single layer of red blood cells fixed on a cover glass was imaged at varying axial positions [Fig. 4(c) and movie S3 in the Supplemental Material [8]]. The stack of the maximum-amplitude projections on the orthogonal plane clearly shows the optical sectioning capability of PI-PAM [Fig. 4(c)].

Finally, we applied PI-PAM to subdiffraction imaging of live rose petal epidermal cells at 570 nm. Pink anthocyanins in cell vacuoles provided the absorption contrast for PA imaging, and they are also commonly used for fluorescence imaging (Supplemental Material, Fig. 4 [8]). In the PA images, densely packed epidermal cells can be clearly resolved. The cell vacuoles are bright, while the cell walls and cell nuclei are dark [Fig. 4(d)]. By z scanning the sample with a step size of 0.5 μm, PI-PAM was performed to

section the cells at different depths [Figs. 4(e) and 4(f) and movie S4 in the Supplemental Material [8]]. With z scanning, PI-PAM has achieved three-dimensional subdiffraction resolution.

In summary, we have demonstrated three-dimensional subdiffraction imaging of both fluorescent and nonfluorescent samples by spatially trimming the excitation volume via the photobleaching effect. We note that PI-PAM can be applied to both fluorescent and nonfluorescent species [9]. When fluorescence is present, it may change the bleaching rate power dependence on the excitation intensity, and thus the resolution improvement. Fortunately, most fluorescent species have a quite low quantum yield (typically less than 10%); therefore, the nonfluorescent bleaching effect still dominates the imaging process.

It is necessary to discuss the bleaching effect on the relative feature contrast between the "bleached region" and "nonbleached region." First, approximately, only the absorbers within the optical focal plane are bleached. When the optical focal plane is moved to other depths, the same bleaching process is repeated and thus the final image contrast between different depths should not be changed. Second, the distortion between the bleached and nonbleached regions can be minimized by reducing the frame numbers or the excitation light intensity. However, this results in reduced SNR as well. In practice, a balance between sample distortion and SNR should be carefully determined. If permanent photobleaching is a concern in the imaging process, the dynamics of reversibly photoswitchable chromophores can be used instead. While the photoswitchable chromophores can be cycled between bright and dark states, the switching rate strongly depends on the switching light intensity [10,11], which provides a zero-loss alternative for PI-PAM.

The same principle of PI-PAM can be readily transferred to fluorescence microscopy, the major imaging tool currently used in biological studies. Because the photobleaching effect occurs in the excitation phase of the imaging process, our method can be applied to confocal microscopy and two-photon microscopy. Compared with other optical imaging modalities, PA detection is not necessarily superior, because each modality has its own unique advantages. Our main purpose is to introduce a subdiffraction imaging method to both PA and other optical imaging communities. Compared with fluorescence microscopy, photoacoustic microscopy can image nonfluorescent species, and can potentially penetrate deeper due to the one-way optical scattering. However, compared with optical imaging where high sensitivity detectors are used, PA imaging suffers from the relatively low SNR due to the less sensitive ultrasonic transducers. To further improve the PA detection sensitivity, more work is necessary to develop optimum illumination and state-of-the-art acoustic detectors [12]. We expect that realizable improvements to the acoustic detector may enable single molecule detection sensitivity, comparable to that of optical detection [12].

---

[*]lhwang@wustl.edu

[1] B. Huang, M. Bates, and X. W. Zhuang, Annu. Rev. Biochem. **78**, 993 (2009).

[2] K. Jacobson, E. Elson, D. Koppel, and W. Webb, Nature (London) **295**, 283 (1982).

[3] I. Rasnik, S. A. McKinney, and T. Ha, Nat. Methods **3**, 891 (2006).

[4] L. Gao, L. Wang, C. Li, A. Garcia-Uribe, and L. V. Wang, J. Biophotonics **6**, 543 (2013).

[5] T. S. Chen, S.-Q Zeng, Q.-M. Luo, Z.-H. Zhang, and W. Zhou, Biochem. Biophys. Res. Commun. **291**, 1272 (2002).

[6] G. H. Patterson and D. W. Piston, Biophys. J. **78**, 2159 (2000).

[7] L. H. V. Wang and S. Hu, Science **335**, 1458 (2012).

[8] See Supplemental Material at http://link.aps.org/supplemental/10.1103/PhysRevLett.112.014302 for detailed derivations of the equations, as well as other supporting notes, methods, figures, and videos.

[9] H. F. Launer, Nature (London) **218**, 160 (1968).

[10] M. Bates, B. Huang, B., G. T. Dempsey, and X. Zhuang, Science **317**, 1749 (2007).

[11] G. H. Patterson, L.-M. Ting, Y. Wang, J. S. Condeelis, and V. V. Verkhusha, Nat. Methods **8**, 771 (2011).

[12] A. M. Winkler, K. Maslov, and L. V. Wang, J. Biomed. Opt. **18**, 097003 (2013).